Earth, Planets and Space

EXPRESS LETTER

Characteristics of the deep sea tsunami excited offshore Japan due to the air wave from the 2022 Tonga eruption

Yuichiro Tanioka[1*], Yusuke Yamanaka[1] and Tatsuya Nakagaki[2]

Abstract

A large eruption of the Hunga Tonga-Hunga Ha'apai volcano in Tonga on January 15, 2022 generated air–sea coupled tsunamis observed at the ocean-bottom pressure sensor network along the Japan Trench (S-net) in Japan. Initial tsunamis from the 2022 Tonga eruption, detected by 106 ocean-bottom pressure sensors, were well modeled by an air–sea coupled tsunami simulation, with a simple atmospheric pressure pulse as sine function, having a half-wavelength of 300 km and a peak amplitude of 2 hPa. A one-dimensional air–sea coupled tsunami simulation having a simple bathymetry shows that an input atmospheric pressure pulse with a short half-wavelength of 50 km, which is shorter than the length of the ocean bottom slopes, caused an amplitude increase via the Proudman resonance effect near the deep trench. The wavefront distortion due to the separation of the air–sea coupled wave propagating with a speed of 312 m/s and tsunami propagating with that of $\sqrt{gd}$, where g is gravity acceleration and d is the ocean depth, is also significant near the shore. In contrast, these effects are not significant for the half-wavelength of the input atmospheric pressure pulse of 300 km. These results indicate that the air–sea coupled tsunami propagating through the trench is sensitive to the wavelength of an atmospheric pressure pulse.

Keywords: 2022 Tonga eruption, Air–sea coupled tsunami, Numerical simulation, Proudman resonance

*Correspondence: tanioka@sci.hokudai.ac.jp
[1] Institute of Seismology and Volcanology, Faculty of Science, Hokkaido University, Sapporo, Japan
Full list of author information is available at the end of the article

Graphical Abstract

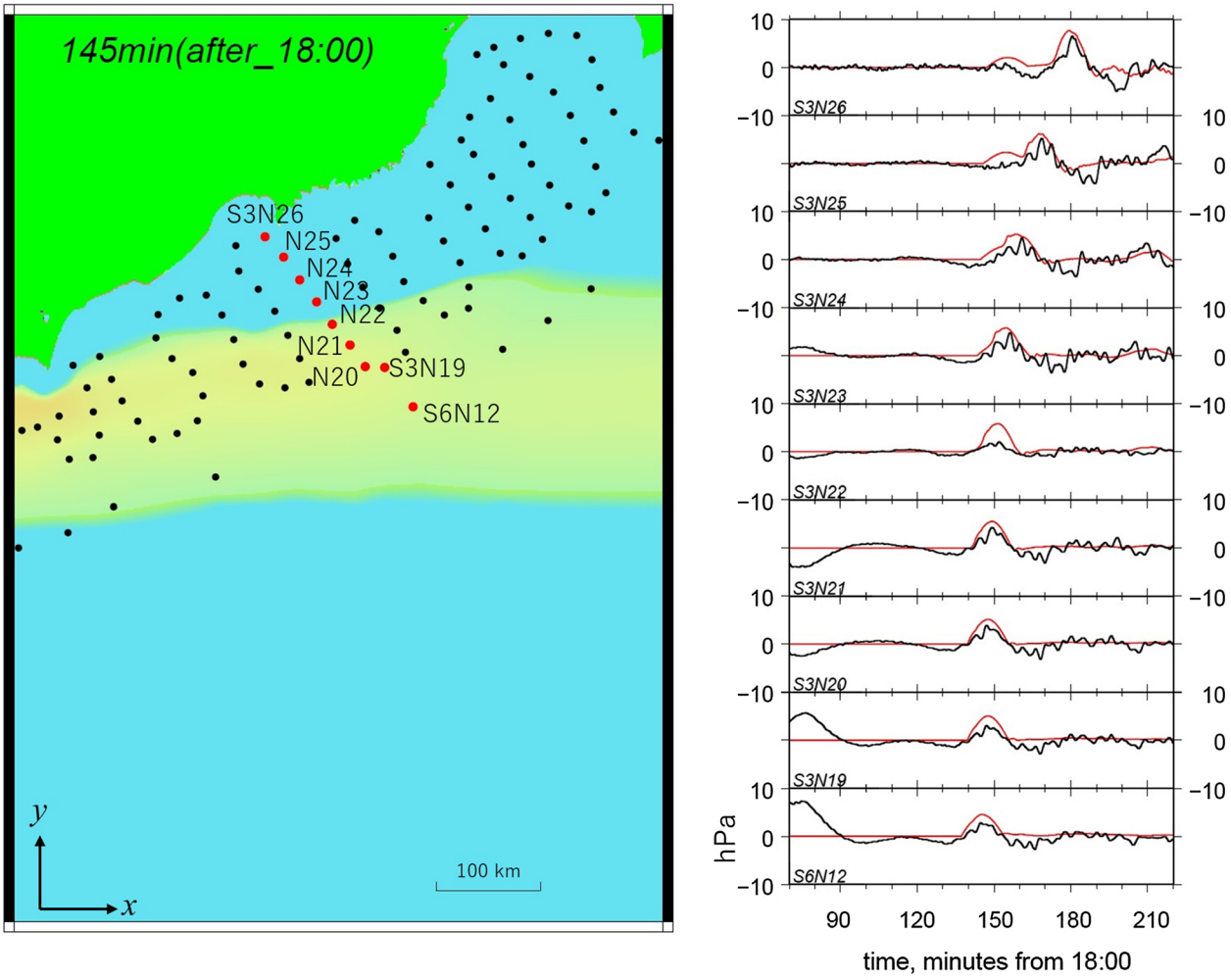

Introduction

A large eruption of the Hunga Tonga-Hunga Ha'apai volcano in Tonga on January 15, 2022, caused devastating disasters in nearby areas. The eruption generated air waves coupled with seawater waves propagating through the Pacific. Tsunamis, long-waves in the ocean, generated by the air wave from the eruption were observed in tide gauges and ocean-bottom pressure sensor network along the Japan Trench (S-net) in Japan. The network, which includes 150 pressure sensors connected by a cable with 30-km intervals, is operated by the National Research Institute for Earth Science and Disaster Resilience (NEID) in Japan (Uehira et al. 2012; Kanazawa 2013). A maximum tsunami amplitude of 1.2 m was observed at Amami in Japan, and thus, a tsunami warning was issued by the Japan Meteorological Agency.

Similar air–sea waves had previously been generated by the Krakatoa volcano eruption in 1883 (Harkrider and Press 1967), and the authors indicated that the air wave propagated at a speed of 312 m/s as the fundamental gravity mode in the atmosphere–ocean system. Nishida et al. (2014) indicated that the atmospheric pressure waves propagating at the acoustic speed were Lamb waves. This kind of air–sea coupled waves, which are often called to meteotsunamis, has already been studied without volcanic eruptions (Hibiya and Kajiura 1982; Fukuzawa and Hibiya 2020; Kubota et al. 2021). Saito et al. (2021) suggested that meteotsunamis are amplified when the velocity of the air waves is similar to that of the tsunami waves. This is called

the Proudman resonance effect (Williams et al. 2021). In the case of the tsunami caused by the air wave from the volcanic eruption, the tsunami propagating near a deep trench should be amplified. Sekizawa and Kohyama (2022) investigated the sea-surface fluctuations by the 2022 Tonga eruption based on a one-dimensional computation.

In this study, the tsunami waves observed at ocean-bottom sensors of S-net in Japan were modeled by the air waves generated by the 2022 Tonga eruption. We discuss the characteristics of tsunami propagation, including the tsunami amplification near the Japan Trench, which has a depth of approximately 8 km.

Data and method

Ocean bottom pressure data observed at 106 out of 150 sensors of S-net (National Research Institute for Earth Science and Disaster Resilience, 2019) were downloaded (Fig. 1). The observed data are filtered in the periods between 100 and 3600 s using the bandpass filter in Seismic Analysis Cord (SAC) developed by Goldstein et al. (2003) (Additional file 1: S1).

The governing equations to be solved by the numerical simulation are briefly explained. With linear approximation, Euler`s momentum equation (Dean and Dalrymple 1991) can be simplified as:

$$\frac{\partial u}{\partial t} = -\frac{1}{\rho}\frac{\partial p}{\partial x}, \tag{1}$$

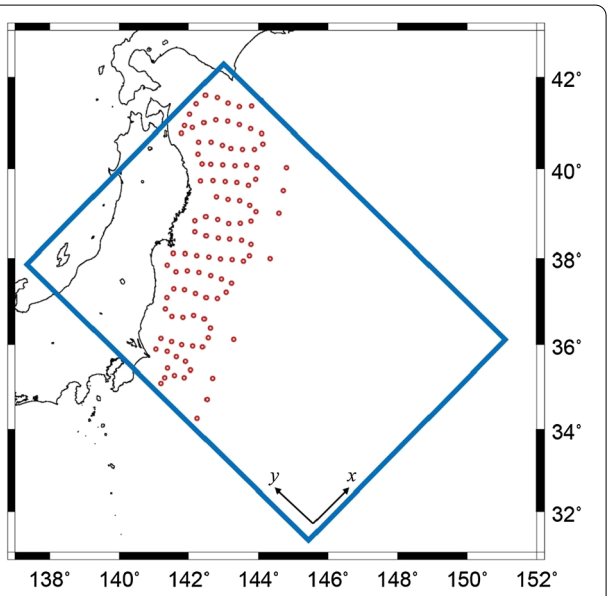

Fig. 1 Location of ocean bottom pressure sensors in S-net (red circle) used in this study. The blue rectangle denotes the air–sea coupled tsunami computation area

$$\frac{\partial v}{\partial t} = -\frac{1}{\rho}\frac{\partial p}{\partial y}, \tag{2}$$

$$\frac{\partial w}{\partial t} = -g - \frac{1}{\rho}\frac{\partial p}{\partial z}, \tag{3}$$

where u, v are the water velocities in the horizontal x, and y-directions, and w is the water velocity in the vertical z-direction (upward positive); p is the pressure, g is gravity acceleration, and ρ is the water density. In longwave theory, the vertical velocity is negligibly small compared with the horizontal velocities: the horizontal velocities in x- and y-directions (u and v) can be approximated to depth-averaged velocities (U and V). Using the former condition, Eq. (3) becomes

$$\frac{\partial w}{\partial t} = -g - \frac{1}{\rho}\frac{\partial p}{\partial z} = 0. \tag{4}$$

Then, pressure p is $p = -\rho g z + c$ based on a vertical integration of Eq. (4), where c is a function of x, y and t. As a boundary condition, pressure (p) is equal to be an atmospheric pressure (p_0) at the ocean surface ($z = h$). Pressure, p, then becomes $p = \rho g(h - z) + p_0$. A value of p_0 is an input to compute air–sea coupled waves. Furthermore, integrating Eqs. (1) and (2) along the depth and using the depth-averaged velocities and pressure, depth-integrated momentum equations in a two-dimensional horizontal plane are obtained as:

$$\frac{\partial U}{\partial t} = -g\frac{\partial h}{\partial x} - \frac{1}{\rho}\frac{\partial p_0}{\partial x}, \tag{5}$$

$$\frac{\partial V}{\partial t} = -g\frac{\partial h}{\partial y} - \frac{1}{\rho}\frac{\partial p_0}{\partial y}. \tag{6}$$

Using a depth integration of the mass conservation equation, the continuity equation becomes

$$\frac{\partial h}{\partial t} = -\frac{\partial (d * U)}{\partial x} - \frac{\partial (d * V)}{\partial y}, \tag{7}$$

where h is the wave height and d is the still water depth. The momentum Eqs. (5) and (6) for air–sea coupled waves and continuity Eq. (7) were numerically solved using a staggered grid system with an input of the atmospheric pressure gradient at each time step. The grid sizes of the numerical computation were set at 1.5 km in both x and y-directions.

The atmospheric pressures observed at approximately 1300 stations in Japan (Weathernews Inc., https://global.weathernews.com/news/16551/, 2022) showed that the pressure pulse (a peak amplitude of approximately 2 hPa, and the duration of 20–15 min) passed

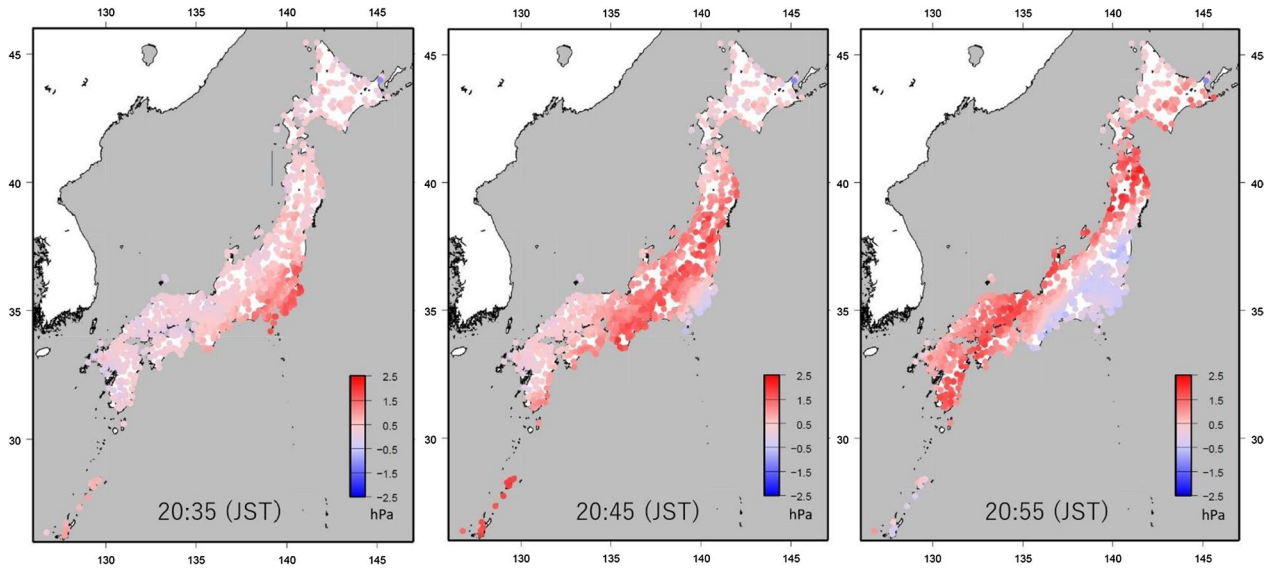

Fig. 2 Three snapshots for the amplitude distribution of pressure changes observed at 1250 stations in Japan (Weathernews Inc., https://global.weathernews.com/news/16551/, 2022) at 20:35, 20:45, 20:55 (Japan Standard Time) in 15th of January

through Japan from southeast to northwest with a strike of − 44°. Figure 2 shows three snapshots of the amplitude distribution of pressure changes observed at those stations at 20:35, 20:45, 20:55 (Japan Standard Time) on the 15th of January. The shape of the pressure pulse was assumed to be half the wavelength of a sine wave. The half-wavelength was set to 300 km, which corresponded to a duration of 16 min using the speed of 312 m/s for the pressure pulse. The peak amplitude was set to 2 hPa. First, numerical computation in one dimension with a constant ocean depth of 5500 m was carried out to obtain the steady state of the air–sea coupled initial wave. The pressure pulse and the steady-state initial wave are entered into the two-dimensional computational domain from the low boundary along the x-axis (Fig. 3). The pressure pulse is continuously propagated in the y-direction with a constant velocity of 312 m/s. The bathymetry was rotated 44° clockwise (Figs. 1, 3) to match a strike of the pressure wave from Tonga. Finally, the observed pressure changes at ocean bottom (p_b) are calculated from the pressure changes due to ocean waves (p_w) and the atmospheric pressure (p_0) pulse as described by Kubota et al. (2021) and Saito et al. (2021):

$$p_b = p_w + p_0 \text{ where } p_w = \rho g h. \quad (5)$$

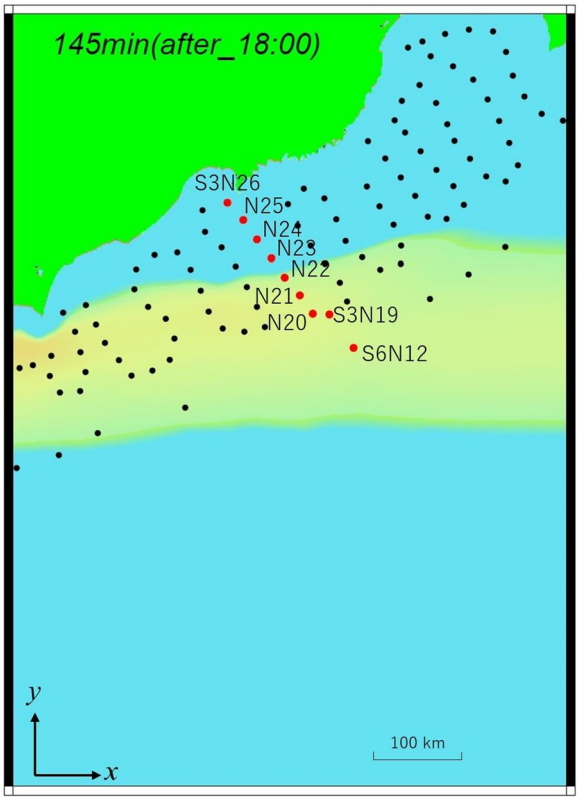

Fig. 3 A snapshot of an air–sea coupled computed tsunami at 145 min after 18:00. Circles represent the locations of ocean-bottom pressure sensors used in this study. Red circles represent the sensors where observed and computed waveforms are compared in Fig. 3

Results

Nine observed pressure changes at stations, S6N12, S3N19, S3N20, S3N21, S3N22, S3N23, S3N24, S3N25, and S3N26 (Fig. 3), are compared with computed

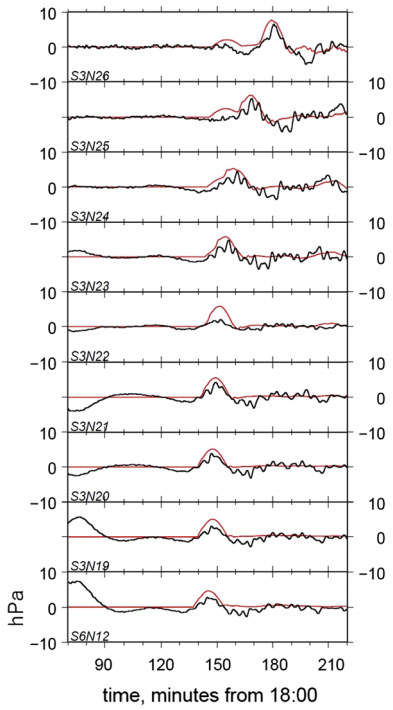

Fig. 4 Comparison of observed and computed waveforms at the nine sensors shown in Fig. 2. Black represents observed waveforms, and red represents computed waveforms. Long-period waves in the first 100 min in the observed waveforms are an effect of the bandpass filter

pressure changes (Fig. 4). In Additional file 1: S1, the observed pressure changes of 106 stations in the S-net are compared with computed pressure changes. The absolute time of the computed pressure changes was set to fit the observed and computed pressure changes at S6N12. Time presented in this paper is Japan Standard Time. The computed waveforms well explain the observed maximum amplitudes and waveforms at all stations. For a typical tsunami caused by an earthquake, shoaling from the deep to the shallow ocean should cause an amplitude increase. A small shoaling effect can be seen for this air–sea coupled tsunami (Fig. 4). The separation of atmospheric pressure and wave pressure changes can be seen at S3N26. The Proudman resonance effect (Williams et al. 2021; Saito et al. 2021), the amplitude increase near the Japan Trench, is difficult to identify by comparing pressure changes at S6N12 and S3N19 in Fig. 4. We performed a one-dimensional simulation on a simple bathymetry to clarify these effects.

One-dimensional tsunami simulation

A one-dimensional tsunami simulation was carried out to understand the tsunami waveform deformation due to the existence of a deep trench. A simple bathymetry was set to compute the tsunami (Fig. 5): a shore 100 km away from the left boundary; a slope of 1/25 from the shore to 300 km away from the boundary, where water depth is 8000 m (trench); a slope of 1/80 from 300 to 500 km away, where the water depth is 5500 m; and a flat bottom from 500 to 1000 km away. For an input of the atmospheric pressure pulse having a peak amplitude of 2 hPa, three different half-wavelengths, 50 km, 100 km, and 300 km, were tested for this simulation.

Red lines in Fig. 5 show snapshots of waveforms at the ocean surface every 200 s for each input wavelength. Black lines in Fig. 5 are the atmospheric pressure changes with the maximum amplitude of 2 hPa. Table 1 shows ratio of the maximum amplitude for each snapshot in Fig. 5 to the maximum amplitude for the input pulse. For a half-wavelength of 50 km (Fig. 5a; Table 1), three snapshots from 600 to 1000 s clearly show that the amplitudes of tsunami increase 1.7 times when the water depths are increased to 8000 m. This is due to the Proudman resonance effect suggested by Williams et al. (2021) and Saito et al. (2021). After 1000 s, the shoaling effect from 8000 m depth to the shore increased the amplitude of tsunami. Shortening of the wavelength by the shoaling is not obvious. However, the shape of the wave front is distorted at 1400 and 1600 s. This is due to the separation of air–sea coupled wave propagating with a speed of 312 m/s and tsunami propagating with that of $\sqrt{gd}$.

For a half-wavelength of 300 km (Fig. 5c), three snapshots from 400 to 800 s show that the shapes of the waves are distorted with time, while the amplitudes of the waves are almost the same, 0.9–1.0 times in Table 1. In contrast, the shoaling effect from 8000 m depth to the shore is clearly seen in both the amplitude increase and wavelength shortening. The distortion of the wavefront at 1600 s is visible but not significant.

The snapshots from a half-wavelength of 100 km (Fig. 5b; Table 1) show that the characteristics of the waveforms are between those for half-wavelengths of 50 and 300 km. Three snapshots from 600 to 1000 s show that the amplitudes of the tsunami increased 1.4 times when the depth of the water increased to 8000 m. The shoaling effect is also observed in both the amplitude increase and wavelength shortening. The distortion of the wavefront is also observed from 1400 to 1800s (Fig. 5b).

Discussion

Although the initial air–sea coupled tsunamis observed at ocean pressure sensors in S-net were well modeled in this study, the origin of large later tsunamis observed along the Japanese coast should be understood clearly for mitigation of future tsunami hazards. For this purpose, the air–sea coupled waves which were generated from

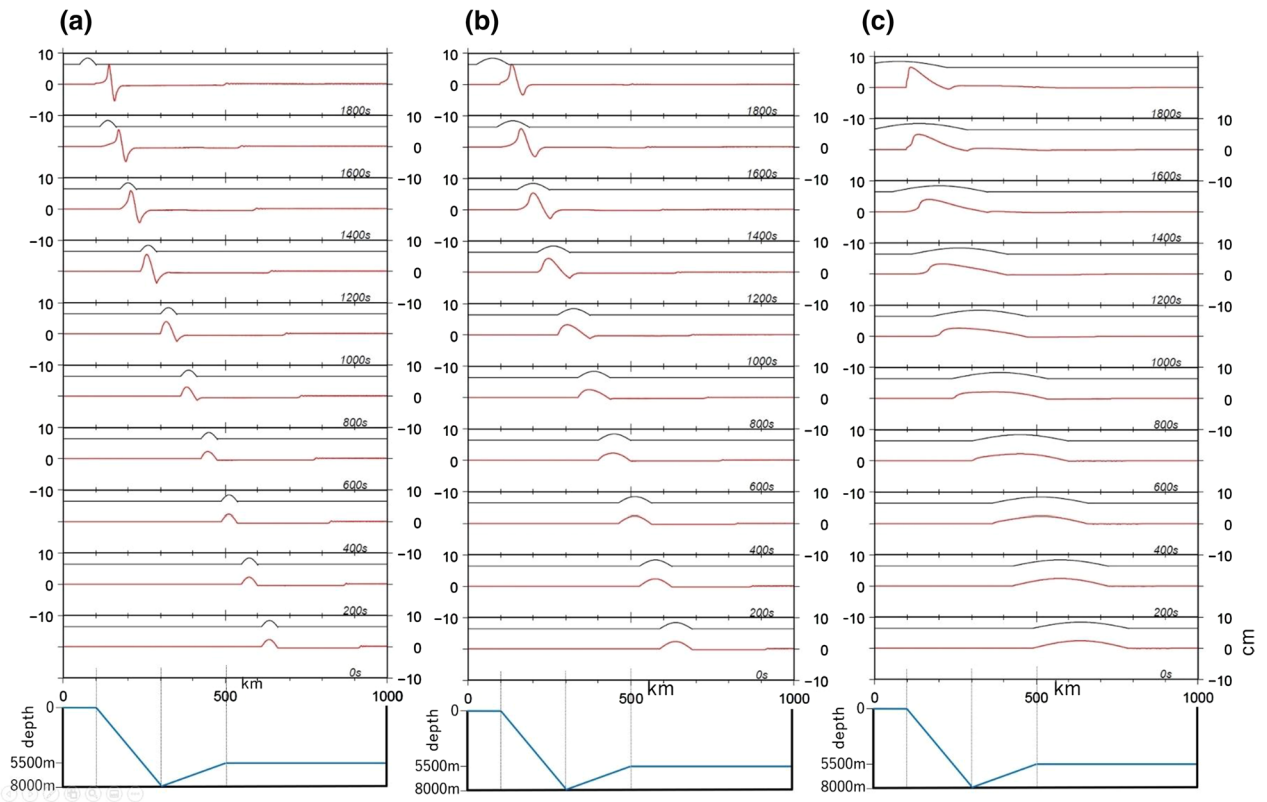

Fig. 5 Ten snapshots (red lines) of one-dimensional air–sea coupled wave simulations for three atmospheric pressure pulses, half-wavelengths of 50 km (**a**), 100 km (**b**), and 300 km (**c**). Black waveforms are the atmospheric pressure changes with the maximum amplitude of 2 hPa for each snapshot. The bottom shows the simple bathymetry used in this simulation

Table 1 Ratio of maximum amplitude for each snapshot in Fig. 5 to that for the input pulse

Time of snapshots in Fig. 5	Ratio of maximum amplitude to the input pulse		
	Half-wavelength 50 km	Half-wavelength 100 km	Half-wavelength 100 km
0 s	1.0	1.0	1.0
200 s	1.0	1.0	1.0
400 s	1.0	1.0	1.0
600 s	1.0	1.0	0.9
800 s	1.3	1.1	0.9
1000 s	1.7	1.4	1.1
1200 s	2.4	1.9	1.4
1400 s	2.7	2.3	1.7
1600 s	2.4	2.5	2.0
1800 s	2.7	2.7	2.7

the eruption at the Hunga Tonga-Hunga Ha'apai volcano and propagated through the Pacific should be properly modeled as a future study.

The shape of the pressure pulse was assumed to be half the wavelength of sine wave in this study. The shape can be significantly affected the air–sea coupled waveforms if more complicated shape of the pressure pulse is generated at the source.

Conclusions

Initial tsunamis from the 2022 Tonga eruption observed at 106 ocean-bottom pressure sensors in S-net, Japan, were well modeled by the air–sea coupled tsunami simulation with an atmospheric pressure pulse having the half wavelength of 300 km and the peek amplitude of 2 hPa.

A one-dimensional air–sea coupled tsunami simulation with a simple bathymetry shows that an input atmospheric pressure pulse with a short half wavelength of 50 km, which is shorter than the length of the slope (200 km), caused an amplitude increase by the Proudman resonance effect near the deep trench. The wavefront distortion due to the separation of the air–sea coupled wave propagating with a speed of 312 m/s and tsunami propagating with that of $\sqrt{gd}$ was also significant near the shore. In contrast, when the half wavelength of the input

atmospheric pressure pulse was 300 km, which is longer than the length of slops, the wave shape distortion due to those effects became small. These results indicate that the air–sea coupled tsunami propagating through the trench is sensitive to the wavelength of an atmospheric pressure pulse.

Supplementary Information

The online version contains supplementary material available at https://doi.org/10.1186/s40623-022-01614-5.

Additional file 1: S1. Comparison of observed and computed waveforms at 106 ocean bottom pressure sensors shown in top-left figure (a). b) Black lines are observed waveforms, red lines are computed waveforms. Station name shown in bottom-left corner. Long-period waves in the first 100 min in the observed waveforms are an effect of the bandpass filter.

Acknowledgements
We thank Dr. N.Y. Chikasada for providing us the information about his S-net data analysis. We thank Dr. S. Lorito, an anonymous reviewer, the vice editor-in-chief, and the editor for useful comments to improve our paper. This study was partially supported by the Ministry of Education, Culture, Sports, Science and Technology (MEXT) of Japan, under its The Second Earthquake and Volcano Hazards Observation and Research Program (Earthquake and Volcano Hazard Reduction Research).

Author contributions
YT overall research and computations. YY provided information about air–sea coupled wave analysis and discussed research objectives. TN processed observed waveform data. All authors read and approved the final manuscript.

Funding
This study was partially supported by the Ministry of Education, Culture, Sports, Science and Technology (MEXT) of Japan, under its The Second Earthquake and Volcano Hazards Observation and Research Program (Earthquake and Volcano Hazard Reduction Research).

Availability of data and materials
None.

Declarations

Competing interests
The authors declare that they have no competing interests..

Author details
[1]Institute of Seismology and Volcanology, Faculty of Science, Hokkaido University, Sapporo, Japan. [2]Graduatte School of Science, Hokkaido University, Sapporo, Japan.

Received: 2 February 2022 Accepted: 30 March 2022
Published: 24 April 2022

References

Dean RG, Dalrymple RA (1991) Water wave mechanics for engineers and scientists. Adv Ser Ocean Eng 2:368. https://doi.org/10.1142/1232
Fukuzawa K, Hibiya T (2020) The amplification mechanism of a meteotsunami originating off the western coast of Kyushu Island of Japan in the winter of 2010. J Oceanogr 76:169–182. https://doi.org/10.1007/s10872-019-00536-3
Goldstein P, Dodge D, Firpo M, Minner L (2003) SAC2000: Signal processing and analysis tools for seismologists and engineers. In: Lee WHK, Kanamori K, Jennings PC, Kisslinger C (eds) The IASPEI International Handbook of Earthquake and Engineering Seismology. Academic Press, London
Harkrider D, Press F (1967) The Krakatoa air-sea waves: an example of pulse propagation in coupled systems. Geophys J Int 13:149–159
Hibiya T, Kajiura K (1982) Origin of the Abiki phenomenon (a kind of Seiche) in Nagasaki Bay. J Oceanogr Soc Japan 38:172–182. https://doi.org/10.1007/BF02110288
Kanazawa T (2013) Japan Trench earthquake and tsunami monitoring network of cable-linked 150 ocean bottom observatories and its impact to earth disaster science. In: Proceedings of the International Conference Underwater Technology
Kubota T, Saito T, Chikasada NY, Sandanbata O (2021) Meteotsunami observed by the deep-ocean seafloor pressure gauge network off northeastern Japan. Geophys Res Lett 48(21):e2021GL094255. https://doi.org/10.1029/2021GL094255
National Research Institute for Earth Science and Disaster Resilience (2019), NIED S-net, National Research Institute for Earth Science and Disaster Resilience. https://doi.org/10.17598/nied.0007
Nishida K, Kobayashi N, Fukao Y (2014) Background Lamb waves in the earth's atmosphere. Geophys J Int 196:312–316. https://doi.org/10.1093/gji/ggt413
Saito T, Kubota T, Chikasada NY, Tanaka Y, Sandanbata O (2021) Meteorological tsunami generation due to sea-surface pressure change: three-dimensional theory and synthetics of ocean-bottom pressure change. J Geophys Res Oceans 126:e2020. https://doi.org/10.1029/2020JC017011
Sekizawa S, Kohyama T (2022) Meteotsunami observed in Japan following the Hunga Tonga eruption in 2022 investigated using a one-dimensional shallow-water model. EarthArXiv. eartharxiv.org/repository/view/3057/
Uehira K, Kanazawa T, Noguchi S, Aoi S, Kunugi T, Matsumoto T, Okada Y, Sekiguchi S, Shiomi K, Shinohara M, Yamada T (2012) Ocean bottom seismic and tsunami network along the Japan Trench. In: Abstract OS41C-1736 presented at 2012 Fall Meeting, AGU
Williams DA, Horsburgh KJ, Schultz DM et al (2021) Proudman resonance with tides, bathymetry and variable atmospheric forcings. Nat Hazards 106:1169–1194. https://doi.org/10.1007/s11069-020-03896-y

Publisher's Note